Title

On modeling subgrid-scale macro-structures in narrow twisted channels

Authors
Li, Zhi
Hodges, Ben R

Publication Date
2020

DOI
10.1016/j.advwatres.2019.103465

Peer reviewed

Dear author,

Please note that changes made in the online proofing system will be added to the article before publication but are not reflected in this PDF.

We also ask that this file not be used for submitting corrections.

Advances in Water Resources xxx (xxxx) xxx

Contents lists available at ScienceDirect

Advances in Water Resources

journal homepage: www.elsevier.com/locate/advwatres

On modeling subgrid-scale macro-structures in narrow twisted channels

Zhi Li*, Ben R. Hodges

Civil, Architectural and Environmental Engineering Department, The University of Texas at Austin, Austin, TX, USA

ARTICLE INFO

Keywords:
Subgrid topography model
Grid alignment
Narrow twisted channel
Subgrid macro-structures
Topographic dissipation

ABSTRACT

Porosity-based subgrid topography models often fail to capture the effects of subgrid-scale topographic features in the interior of coarse grid cells. Existing approaches that modify bottom roughness or a drag coefficient are inadequate for macro-structures (large emergent or submerged obstacles) in subgrid-scale narrow twisted channels. Such structures partially block the cross-sectional area and provide enhanced topographic dissipation – effects that are not well represented by a drag coefficient that scales on a coarse-grid cell-averaged velocity and the cell volume. The relative alignment between mesh and flow further complicates this problem as it makes the subgrid model sensitive to mesh design. In the present study, three new approaches for simulating subgrid-scale macro-structures in narrow channels are proposed. The interior partial-blocking effect of structures is modeled as reduction of grid face-area. The sheltering of flow volumes around obstacles, which leads to topographic dissipation, is modeled by reducing the cell volume in the momentum equation (only). A mesh-shift procedure is designed to optimize mesh alignment for identifiable subgrid features. Combining the three subgrid methods improves the approximation of surface elevation and in-channel flow rate with a coarse-grid model. Tests are conducted for channelized flow using both synthetic domains and real marsh topography. The new methods reduce the overall mesh dependency of the subgrid model and provides stronger physical connection between effects of macro-structures and their geometry at coarse grid scales.

1. Introduction

Two-dimensional (2D) depth-integrated hydrodynamic models have been used to study salinity transport, evaluate hydrological modifications, and help restoring ecosystems at shallow estuaries and coastal marshes (e.g., Inoue et al., 2008; Matte et al., 2017; Zacharias and Gianni, 2008). The model domains are often characterized by frequent wetting/drying and complex flow paths of various spatial scales, which requires careful selection of an appropriate grid resolution that resolves important topographic features. Unfortunately, in practical applications the grid resolution is often limited by the available computational power. Modeling at coarse resolution (relative to the scales of smallest channels) leaves small-scale topographic features unresolved, leading to errors in modeled surface connectivity, inundation area, and flow rates (Li and Hodges, 2018; 2019).

To improve results for practical coarse-grid simulations, subgrid topography models have been previously proposed to represent the large-scale effects of subgrid-scale features. Such models have been developed for efficient modeling of estuarine hydrodynamics (e.g. Wu et al., 2016; Sehili et al., 2014) and urban flooding (e.g., Sanders et al., 2008; Guinot et al., 2017). One popular type of subgrid models parametrizes the high-resolution topography as a "porosity" term similar to the approach for handling spatial hetereogeneity in groundwater models (e.g., Defina et al., 1994; Defina, 2000; Bates, 2000). Two types of porosities have been identified and used in the prior literature: the volumetric porosity (fraction of cell volume occupied by water) and the areal porosity (fraction of cell face area occupied by water). The former is used to adjust cell storage and the latter is used to adjust conveyance (i.e., flow rate) through cell faces (Sanders et al., 2008). Although porosity-based subgrid models can capture the changes of cell storage and flow conveyance across the cell faces, they ignore the contribution from topographic features in the interior of a coarse cell. For general topography with wetting/drying, Li and Hodges (2019) designed a combined volume-area subgrid model that automatically preserves high-resolution surface connectivity, thereby allowing more than 30 $\times$ grid coarsening while maintaining complex connectivity patterns.

Arguably, the variability of structural scales in a marsh is fractal – from the winding of the channels themselves to the bank shapes and on down to the rocks, plants, stems, and leaves that affect fluid flow. We propose separating this structural space based on scales that can be modeled, scales that can be observed, and scales that are unknown. As a convenient set of equivalent definitions, a physical feature of length scale ℓ can be categorized as either (i) resolvable, (ii) macro-structure, or (iii) micro-structure. If we take a practical model grid scale as Δx (whereas topography data is available at a finer grid scale δx), the re-

* Corresponding author.
E-mail address: zhili@utexas.edu (Z. Li).

https://doi.org/10.1016/j.advwatres.2019.103465
Received 19 July 2019; Received in revised form 9 November 2019; Accepted 12 November 2019
Available online xxx

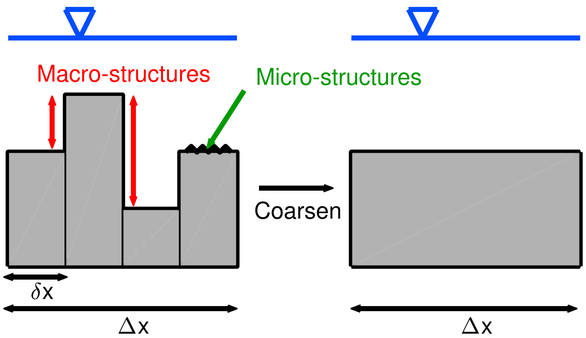

Fig. 1. A coarse grid cell containing four subgrid macro-structures ($\Delta x/\delta x = 4$) whose effects must be represented on the Δx model grid.

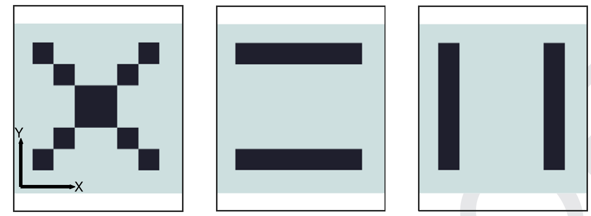

Fig. 2. Theoretical arrangement of 12 emergent macro-structure elements in the interior of a coarse grid that would have significantly different flow effects. Light color represents the background topography and dark color represents emergent macro-structures. The three coarse grid cells have identical volumetric and areal porosities.

solvable features are those of $\ell \geq \Delta x$ that can be directly represented in the model. The macro-structure features are those that are identifiable with available data between scales $\Delta x > \ell \geq \delta x$ and could be resolved in the model if we had sufficient computational power. The micro-structure are features $\ell < \delta x$ that are relatively unknown and constitute "roughness". For example, airborne lidar data readily provides $\delta x \sim 1$ m digital terrain that identifies physical structures over the wide expanse of a coastal marsh, but it is typically impractical to model hydrodynamics with today's computers at much less than a $\Delta x \sim 10$ m grid scale. Arguably, smaller-scale features such as plant topology are identifiable through structure-from-motion and land-based 3D lidar, but such methods are presently impractical over large areas and thus such features constitute micro-structure. The intersection of practical data collection scales and practical modeling scales set the boundaries between resolvable, macro-, and micro-scale features (Fig. 1).

There are two major challenges associated with this conceptual model in a shallow 2D system: (i) upscaling of micro-structure drag, and (ii) upscaling of macro-structure flow effects. The two issues are closely related because the macro-structure channelizes flow and controls the subgrid spatial velocity distribution, which affects the micro-structure drag. The effects of micro-structures on an overlying shallow flow (at scale δx) are reasonably modeled using bottom roughness (e.g., Manning's n) that in 2D relates the depth-integrated drag force to the bottom stress characterized by the depth-averaged velocity – where both are considered only over a subgrid area $\delta x \times \delta x$. However, exact upscaling of the drag force from the δx subgrid scale to the coarse-grid Δx scale requires the subgrid spatial velocity distribution, which is unknown. Approximate upscaling is typically accomplished by introducing calibration parameters (Ozgen et al., 2015), assuming constant friction slope (Volp et al., 2013; Wu et al., 2016; Shin, 2016), or assuming a uniform flow direction at the δx scale (Duan et al., 2017). Unfortunately, in a shallow coastal marsh (as investigated herein) the spatial heterogeneity of subgrid channels cannot be adequately represented with the prior techniques. The underlying difficulty in this research area is that we do not have a comprehensive theory of fluid-structure interaction that provides the robustness of the kinetic energy/length scale relationship in turbulence modeling, e.g., as for plane jets and mixing layers in the ubiquitous $k-\epsilon$ turbulence model (Launder and Spalding, 1974). Thus, both the present and prior works rely on scalings that represent observable features and require the introduction of parameters that *cannot* be reduced to standard coefficients such as von Karman's κ or the C_μ, C_1, and C_2 that are standardized and used in $k-\epsilon$ subgrid models for a wide range of turbulence conditions.

Macro-structures are not necessarily random roughness elements and hence their anisotropic distribution affects the flow within a coarse-grid cell. For example, consider Fig. 2 that shows three coarse-grid cells with uniform bathymetry that is confounded by emergent macro-structure. These imaginary configurations are designed such that the volumetric porosity of the macro-structures are identical. Furthermore, as there are no edge blockages the face areal porosities are also identical. Nevertheless, it should be obvious that the different distributions of macro-structure will have significantly different effects on the overall flow through the coarse-grid cell. The cell in the left panel has an isotropic arrangement of the macro-structures, which generates similar resistance to incoming flow in both x and y directions. The middle panel is expected to have similar effects to the left panel for flow in the y direction, but has minimal resistance to flow in the x direction. Conversely, the right panel provides a preferential flow path in the y direction and slows flow in the x. An upscaling model needs to represent the anisotropic and heterogeneous effects of these structures on the flow field. The real-world problem becomes even more complicated as the macro-structures are rarely vertically uniform but have different horizontal areas at different vertical levels. Thus, changes in the water level (i.e., wetting/drying) can change the effective shape, drag, and flow connectivity through the macro-structure.

Prior subgrid models typically relate macro-structures to bottom stress and treat the coarse-grid drag coefficient C_D as a calibration parameter (e.g. Sanders et al., 2008; Ozgen et al., 2016a; 2016b; Bruwier et al., 2017; Guinot et al., 2017; 2018). However, an effective theoretical linkage between a drag coefficient and the arbitrary 2D geometry of the macro-structures remains to be found. On the most fundamental level, if the size of a macro-structure is comparable to flow depth (the "low-submergence condition"), its bottom stress cannot be represented using Manning-type formulas (Katul et al., 2002; Cea et al., 2014; Cheng, 2015). Although other theories have been suggested for estimating drag coefficient – e.g., the use of turbulence mixing-layer theory (Casas et al., 2010) – a robust well-accepted alternative has not been found (Powell, 2014). Furthermore, macro-structures induce a variety of phenomena via mechanisms other than drag – e.g., sidewall obstructions (Azinfar and Kells, 2009) and momentum dissipation due to reflection of positive waves (Guinot et al., 2017) – that are not well-represented by a drag-law paradigm. Finally, it has been observed that the spatial heterogeneity of macro-structures cannot be fully captured through global calibration with one or two simple parameters (D'Alpaos and Defina, 2007; Horritt and Bates, 2001) and the complexity of geometry over an entire marsh make it impossible to obtain sufficient flow data for optimized local adjustment of calibration parameters (Li and Hodges, 2018).

To address the challenges discussed above, the present work builds on the subgrid blocking algorithm of Li and Hodges (2019), which preserves subgrid connectivity, and the porosity-based approaches of Sanders et al. (2008); Guinot et al. (2017) and Bruwier et al. (2017), which apply anisotropy in the porosity to represent coarse-grid interior and face-based effects. Herein we focus on sidewall macro-structures in the narrow twisted channels of shallow coastal marshes, where two issues (other than drag) associated with subgrid macro-structures are identified: (i) grid alignment and (ii) topographic dissipation. As a brief overview, the former issue arises because subgrid methods depend on the relationship between mesh faces and the macro-structures such that shifting the mesh can alter the number of macro-structure sub-elements in a given coarse-grid cell. To use this property to our advantage, a mesh-adjustment method is developed to rectilinearly shift the uniform coarse-grid mesh into an optimum placement that provides the minimum number of cells that are “barely wet.” The latter issue (topographic dissipation) is addressed in a new approach to coarse-grid upscaling of high-resolution topography (i.e., modifying formulation of the porosities) based on quantifications of the macro-structure geometry. The new methods are evaluated using both simple straight channels and real marsh channels. Compared to simple calibration using C_D, the new geometry-based representation of macro-structures provides a stronger physical connection between flow and topography, albeit at the additional complication of introducing a new parameter (γ, see Section 2).

A brief background of the numerical model, existing issues with topographic dissipation and grid alignment are provided in Section 2, together with description of the new subgrid methods that handles these issues. Test cases and results are described in Section 3. Discussions on model achievements, limitations and possible future directions are provided in Section 4. Our conclusions are presented in Section 5.

2. Methods

2.1. Hydrodynamic model

The present work builds on the subgrid method (SB) previously developed and implemented in the *FrehdC* model, which is explained in detail in Li and Hodges (2019) and briefly below. The *FrehdC* model is the C-language version of the Fine Resolution Environmental Hydrodynamic Model (*Frehd*), which was originally programmed in Matlab. The latter model inherits works by Hodges et al. (2000); Hodges (2004); Rueda et al. (2007); Hodges and Rueda (2008); Wadzuk and Hodges (2009); Hodges (2014, 2015); Li and Hodges (2018). The original *Frehd* code has been streamlined, parallelized, and reduced in options so that *FrehdC* efficiently solves the 2D depth-integrated free surface continuity equation, the momentum equations, and the scalar transport equation. These equations can be written in the volume-integrated form as:

$$\frac{\partial}{\partial t}\int_{\Omega}\eta d\Omega + \int_{\Gamma}\boldsymbol{u}\cdot\boldsymbol{n}dA = 0 \tag{1}$$

$$\int_V\left(\frac{\partial \boldsymbol{u}}{\partial t} + (\boldsymbol{u}\cdot\boldsymbol{n})\frac{\partial \boldsymbol{u}}{\partial \boldsymbol{x}}\right)dV = \int_{\Gamma} g\eta\boldsymbol{n}dA + \int_{\Gamma}\boldsymbol{\tau_v}\cdot\boldsymbol{n}dA + \int_{\Omega}\boldsymbol{\tau_b}d\Omega \tag{2}$$

$$\frac{\partial}{\partial t}\int_V C\,dV + \int_{\Gamma}(\boldsymbol{u}\cdot\boldsymbol{n})C\,dA = \int_{\Gamma}\boldsymbol{\tau_\kappa}\cdot\boldsymbol{n}\,dA \tag{3}$$

where η is the free surface elevation, $\boldsymbol{u} = [u, v]^T$ are depth-averaged velocities, $\boldsymbol{x} = [x, y]^T$ are the corresponding Cartesian axes, $\boldsymbol{n}$ is the normal unit vector, $\boldsymbol{\tau_b}$ is the bottom stress, $\boldsymbol{\tau_v}$ is the viscous stress, C is scalar concentration, $\boldsymbol{\tau_\kappa}$ represents scalar diffusion, dV is an infinitesimal volume inside the model domain (Ω) and dA is an infinitesimal face area, which can be written as $dA = h(\Gamma)d\Gamma$ where $h(\Gamma)$ is the depth function along a volume boundary Γ.

The bottom stress in Eq. (2) is modeled using:

$$\boldsymbol{\tau_b} = \frac{1}{2}C_D\boldsymbol{u}|\boldsymbol{u}| \tag{4}$$

$$C_D = \frac{g\tilde{n}^2}{\bar{H}^{\frac{1}{3}}} \tag{5}$$

$$\bar{H} = \begin{cases}\frac{V}{A_Z}, \text{with SB method}\\ \eta - z_b, \text{otherwise}\end{cases} \tag{6}$$

where C_D is the drag coefficient, $\tilde{n}$ is the constant Manning's roughness coefficient ($\tilde{n} = 0.03$ in this study). If the subgrid model is activated, $\bar{H}$ is the cell-averaged depth, V is the cell volume and A_Z is the free surface area. Both V and A_Z are computed from the high-resolution topography data as illustrated in Li and Hodges (2019). If the subgrid model is turned off, then $\bar{H} = H = \eta - z_b$, where z_b is the bottom elevation of a grid cell.

Although physical viscosity and diffusion are important processes in a shallow marsh, they are predominantly determined by physics at the subgrid scale and are dominated by the numerical dissipation and diffusion in a coarse-resolution model (Li and Hodges, 2018; 2019). As such, we focus our new methods on handling the critical issue of macro-scale effects of advection and reserve the study of macro-scale dissipation and diffusion as a subject for future research.

In traditional structured-grid models without subgrid topography (e.g., Hodges et al., 2000), a grid cell is typically described by a uniform bottom elevation z_b and grid sizes Δx, Δy, such that the horizontal water surface area at any free-surface elevation (η) is $\Delta x\Delta y$, the cell volume is $(\eta - z_b)\Delta x\Delta y$, and the cell face areas are $(\eta - z_b)\Delta y$ and $(\eta - z_b)\Delta x$. Arguably, the next level of complexity for modeling topography with a structured grid is that invoked by our SB method, where the grid cell topography is described using four subgrid variables that are all discrete functions of η: cell volume $V(\eta)$, surface area $A_Z(\eta)$, and side face areas $A_X(\eta)$, $A_Y(\eta)$. Similar to the artificial porosities used in other subgrid models (e.g., Ozgen et al., 2016a; Guinot et al., 2018), these variables are calculated from high-resolution topographic data over the range of possible values of η.

Following Casulli (1990), Casulli and Cattani (1994), and Li and Hodges (2019), Eqs. (1) and (2) can be written in discretized forms with embedded subgrid variables. For simplicity in exposition, these can be presented for the inviscid 1D case as:

$$\eta_i^{n+1}(A_Z)_i^n = \eta_i^n(A_Z)_i^n + \Delta t\left(u_{i-\frac{1}{2}}^{n+1}(A_X)_{i-\frac{1}{2}}^n - u_{i+\frac{1}{2}}^{n+1}(A_X)_{i+\frac{1}{2}}^n\right) \tag{7}$$

$$u_{i+\frac{1}{2}}^{n+1} = -g\Delta t K_{i+\frac{1}{2}}^n\frac{(A_X)_{i+\frac{1}{2}}^n(\eta_{i+1}^{n+1} - \eta_i^{n+1})}{V_{i+\frac{1}{2}}^n} + K_{i+\frac{1}{2}}^n E_{i+\frac{1}{2}}^n \tag{8}$$

where i is the cell center index, $i + \frac{1}{2}$ indicates variables stored at cell faces, n represents the time level when appears as superscript (different from Manning's $\tilde{n}$), K and E represent an inverse drag term and an explicit momentum source term that can be written as:

$$E_{i+\frac{1}{2}}^n = u_{i+\frac{1}{2}}^n - \Delta t u_{i+\frac{1}{2}}^n\frac{u_{i+\frac{1}{2}}^n - u_{up}^n}{\Delta x} \tag{9}$$

$$K_{i+\frac{1}{2}}^n = \left(1 + \Delta t\frac{C_D(A_Z)_{i+\frac{1}{2}}^n\sqrt{(u_{i+\frac{1}{2}}^n)^2}}{2V_{i+\frac{1}{2}}^n}\right)^{-1} \tag{10}$$

In Eq. (9), the first-order upwind scheme is used for the advective stencil as higher-order stencils are restricted by insufficient grid resolution in narrow channels (Li and Hodges, 2018). The variable u_{up}^n is the velocity at an upwind face, which could be $u_{i-\frac{1}{2}}^n$ or $u_{i+\frac{3}{2}}^n$ depending on the flow direction. It should be noted that following Li and Hodges (2019), the volumes in momentum (Eqs. (8), (10)) are “staggered”, i.e., they are defined at the cell faces. This leads to different volumes in x and y directions ($V_{i+\frac{1}{2},j}$ versus $V_{i,j+\frac{1}{2}}$) for a 2D stencil. For simplicity in notation, in the following sections we use $V_X = V_{i+\frac{1}{2},j}$ and $V_Y = V_{i,j+\frac{1}{2}}$ to represent the volumes in x, y directions for calculating momentum transport. This staggered volume approach does not affect mass conservation because the cell volume for calculating cell storage is still defined at a cell center.

Following the standard semi-implicit approach (e.g., Casulli, 1990), Eq. (8) is substituted into Eq. (7) to generate a linear system for η^{n+1}. Back-substitution of the linear solution into Eq. (8) provides the updated u^{n+1}. Subgrid variables are updated using η^{n+1} at each time step and hence are treated explicitly (e.g., A_X^n during the $n \to n+1$ solution step), which is consistent with the explicit treatment of Δz in Casulli and Cattani (1994) as discussed in Hodges (2004). Scalar transport is simulated as advective (first-order upwind) and diffusive transport of scalar mass flux, which guarantees mass conservation.

Two features introduced in the Li and Hodges (2019) SB method and used herein are (i) a "block-checking" algorithm that reconstructs the subgrid-scale water-blocking features that are smoothed during grid coarsening, and (ii) setting the bottom elevation of a coarse grid to be the minimum bottom elevations of all its subgrids. The block-checking algorithm eliminates extraneous flow paths that are created due to removal of blocking features in upscaling the grid. Using the minimum bottom elevation is a complementary function as it ensures that actual flow paths are *not* removed during upscaling. As a result, the high-resolution connectivity patterns are preserved in Li and Hodges (2019) at a large grid-coarsening ratio ($r = \Delta x/\delta x \gg 1$). Compared to structured-grid models that do not parameterize subgrid-scale topography, Li and Hodges (2019) showed the SB method provides a better approximation of surface elevation, inundation area, flow rate, and salinity at coarse grid resolution. The SB method is used as a baseline for improvement in the present work.

2.2. Partial blocking and topographic dissipation

2.2.1. Background

The underlying hypothesis of the present work is that the SB subgrid method, as discussed above, can be further improved by simulating the effects of interior macro-structures on the local flow field. Our contention is that one key feature missing in the SB (and other subgrid) method is the tendency of interior macro-structures to contract/expand cross-sectional areas of narrow channels. Such changes create shelter areas (e.g., recirculation zones) in which flow decelerates, leading to an increased velocity gradient across the channel breadth. This phenomenon can be viewed as enhanced "topographic dispersion" of momentum. By applying the SB method at coarse resolution, only one velocity is allowed to exist on each cell face (Guinot et al., 2018), which implies any velocity gradient in the cell interior will be smoothed, resulting "topographic dissipation" – i.e., the integrated kinetic energy of the average velocity, $\bar{u}^2 A$, is less than that implied by the velocity profile $\int u^2\, dA$. The concept of topographic dissipation is applicable beyond recirculation zones and will be a factor wherever there are substantial real-world velocity gradients across a coarse-grid cell. Unless narrow channels are substantially wider than the coarse-grid scale, upscaling high-resolution topography will always lead to insufficient grid resolution across a channel breadth. Thus, the complex geometry of channel boundaries is an important component of the subgrid macro-structures that affect flow (Horritt et al., 2006). Twists and turns of channel boundaries as well as subgrid-scale sidewall obstacles (e.g., bridge piers or natural contraction/expansion of channels) lead to non-uniform velocity distributions and topographic dissipation.

An example of flow at a highly-resolved grid cell that cannot be correctly resolved at a coarse grid (an hence implies topographic dissipation) is shown in Fig. 3a, where a coarse $r = 100$ mesh is overlapped with high-resolution simulation results in a straight channel with a sidewall obstacle (the macro-structure) that contracts cross-sectional area. A recirculation zone is found downstream of the macro-structure where the channel width expands. The high velocities are observed around the channel centerlines and away from the macro-structure, low velocities are observed in the recirculation zone. The expected physical result is stronger momentum transport around the centerline (conveniently referred to as the "advection zone") accompanied by weaker momentum transport in the recirculation zone and turbulent mixing at the interface of the two zones (Han et al., 2017). For illustrative purposes, we can ignore the turbulent mixing layer and consider frictionless inviscid flow in two distinct zones (advection and recirculation zones) in a coarse grid cell, as shown in Fig. 3b. Here we model the flow as only in the x direction. Recall that momentum equation (Eq. (2)) in x direction can be written in the form of the Newton's second law:

$$a_x = \frac{\sum F_{bx}}{\rho V_X} = \frac{\sum (F_{bx})_{\mathrm{adv}} + \sum (F_{bx})_{\mathrm{rec}}}{\rho (V_{X(\mathrm{adv})} + V_{X(\mathrm{rec})})} \tag{11}$$

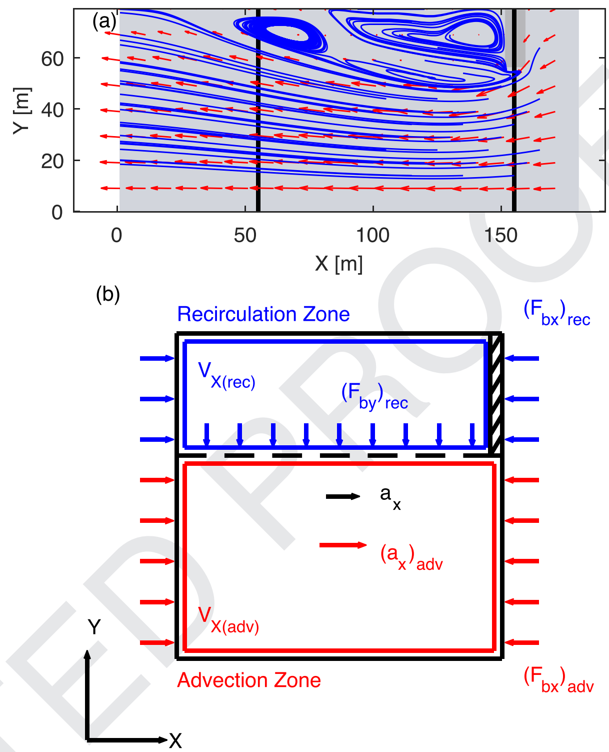

Fig. 3. (a) An example of velocity field and streamlines affected by the macro-structures. The simulation was performed at $\delta x = 1$ m, but the results are displayed at a coarser grid resolution for clarity. Black lines represent a $\Delta x = 100$ m coarse grid. (b) Force balance for advection and diffusion zones in a coarse grid cell (similar to the center cell with sidewall obstacle in (a)) with two different estimates of fluid deceleration, a_x, and $(a_x)_{adv}$. Note that the dimensions and positions of the two zones are sketched for illustration purposes only. In a real channel, these depend on the geometry of the macro-structure as well as the flow field. The reaction forces are not labeled.

where F_{bx} is the barotropic force acting on volume V_X in x direction and subscripts "adv" and "rec" indicate values in the advective and recirculation zones, respectively. The recirculation zone generated due to the macro-structures has negligible mean velocity as the macro-structure exerts reaction forces against incoming flow thereby canceling the barotropic force, which is an argument similar to that used for the interior pressure term of Sanders et al. (2008); Ozgen et al. (2016a). It is thus reasonable to neglect the barotropic force on the recirculation zone and rewrite the Newton's law as:

$$a_x = \frac{\sum (F_{bx})_{\mathrm{adv}}}{\rho (V_{X(\mathrm{adv})} + V_{X(\mathrm{rec})})} \le (a_x)_{\mathrm{adv}} = \frac{\sum (F_{bx})_{\mathrm{adv}}}{\rho V_{X(\mathrm{adv})}} \tag{12}$$

The above implies that topographic dissipation is caused by uniformly distributing the force $\Sigma(F_{bx})_{\mathrm{adv}}$ over the volume of the entire coarse cell. Thus, a coarse cell with interior change of cross-sectional area can be characterized by considering the advection zone alone, and neglecting the recirculation zones that have minimal participation to the momentum transport. This effect can be achieved by replacing (e.g.) $V_{i+1/2}$ and $(A_X)_{i+1/2}$ in momentum and continuity, Eqs. (7) and (8) by the advective volume and advective cross-sectional area. The former is used to constrain excessive topographic dissipation and the latter is used to represent a "partial blocking" effects caused by the reaction forces. Unlike complete blocking of channel's cross section, which has been handled in Li and Hodges (2019), partial blocking does not completely eliminate surface connectivity but reduces channel conveyance as part of the cross section is blocked by the macro-structure.

2.2.2. Method: Effective volume and effective area

To model effects of topographic dispersion (and counteract topographic dissipation), we argue the net force in the x direction at a coarse-grid cell face is applied over an effective volume $V_{X(\text{eff})}$ that is less than the full volume around the face, V_X. A similar argument applies for V_Y. The effective volume only includes regions where strong momentum fluxes are present, neglecting regions like recirculation zones where velocities are small. In the present study, we adopt the simplification made in Fig. 3, where a coarse cell is split into distinct advection and recirculation zones. The effective volume equals the volume of the advection zone, $V_{X(\text{adv})}$. In x direction, the effective volume is calculated as:

$$V_{X(\text{eff})} = \begin{cases} A_{X(\text{eff})}\Delta x, & \text{if } A_{X(\text{eff})} < A_X \\ V_X, & \text{otherwise} \end{cases} \tag{13}$$

where, $A_{X(\text{eff})}$ is the effective area that represents reduction in the cross-sectional area caused by partial-blocking. According to Bruwier et al. (2017), the effective area equals the minimum cross-sectional area across the grid cell, $A_{X(\min)}$. In the present study, we propose $A_{X(\text{eff})} \geq A_{X(\min)}$ with the equality holds only when certain conditions are met (see §2.3 for detailed formulation). The effective volume is different from the original face volume V_X only when $A_{X(\text{eff})} < A_X$; i.e., this approach assumes significant recirculation zones are generated only with severe contractions of the channel's cross-sectional area (as the case shown in Fig. 3). The similar equation for $V_{Y(\text{eff})}$ is readily deduced from the above.

The use of Eq. (13) simulates topographic dispersion caused by increased transverse velocity gradients at channel contractions. However, poorly-represented transverse velocity gradients also exists near the channel boundary walls, even without substantial channel contractions. Simulations performed at coarse resolution inevitably smooth this velocity gradient, leading to further topographic dissipation. A possible consequence of neglecting this near-wall velocity gradient is that topographic dissipation might not be completely suppressed with Eq. (13) alone. To test this concept, we also evaluate an alternative formula for calculating face volumes based on minimum areas as:

$$V_{X(\min)} = \begin{cases} A_{X(\min)}\Delta x, & \text{if } A_{X(\min)}\Delta x > \alpha V_X \text{ or } A_{X(\text{eff})} < A_X \\ \alpha V_X, & \text{otherwise} \end{cases} \tag{14}$$

where α is a model parameter. The idea for this formulation arises from the observation that topographic dissipation can be mathematically countered by reducing the volumes in momentum Eq. (11). Instead of using a smaller volume only at channel contractions – as implied by Eq. (13), the (staggered) face volumes for all cells are replaced by the minimum volumes, $V_{X(\min)}$, calculated from Eq. (14), which should provide higher velocities and weaker dissipation than Eq. (13). The $0 \leq \alpha \leq 1$ parameter in this approach sets a lower limit of $V_{X(\min)}$, which is necessary to avoid instabilities as $V \to 0$. The present study uses $\alpha = 0.7$, which is obtained from a sensitivity study (results not shown). It should be noted that Eq. (14) is certainly not an ultimate solution to topographic dissipation. The use of minimum volume and α are only considered a primitive attempt that shows the possibility of suppressing dissipation by reducing volume, but the exact amount of reduction remains further investigation (also discussed in Section 4.2).

2.3. Effects of grid alignment

2.3.1. Background

Subgrid models are often sensitive to mesh design. If a macro-structure intersects with a cell face (or edge), its partial-blocking effect can be directly simulated using areal porosity (Sanders et al., 2008). Specifically, the grid face area (or areal porosity) is reduced to model decrease in conveyance across the face. However, if the mesh is shifted such that the entire macro-structure is located in the cell interior then a face-based partial-blocking algorithm cannot capture the conveyance effects (Guinot et al., 2017). Grid alignment sensitivity means that a small shift of the mesh position over the high-resolution topography can cause a large change in the areal porosity (A_X, A_Y) and hence a change in the simulation results. We have found this to be the case with the baseline SB model of Li and Hodges (2019) applied to simulations in the Nueces River Delta (Texas, USA). Note that the drag coefficient cannot be used to compensate for misrepresentation of the cross-sectional flow area when the mesh is shifted. That is, the face flow area appears in both continuity (Eq. (7)) and the barotropic term of the momentum equation (Eq. 8), whereas the drag term appears only in the momentum equation (Eq. (8)). Even if we were able to reproduce the same model outcomes as those with unshifted mesh by adjusting drag coefficient, it would certainly be through completely different mechanisms, i.e., getting the "right" answer for wrong reasons – which has limited physical significance (Lane, 2005). Thus, shifting a mesh to move a macro-structure from the face to the interior requires some modification of (e.g.) A_X and/or V_X to compensate if we seek results that are (relatively) insensitive to the mesh alignment.

To address issues of grid alignment, Bruwier et al. (2017) suggested using the minimum areas ($A_{X(\min)}$ and $A_{Y(\min)}$ in x and y directions respectively) across a coarse cell to represent face areas (or areal porosities). With their approach, reduction of face area and the associated change in the reaction force are always captured regardless of the location of macro-structures. Unfortunately, their method did not completely remove mesh-dependency in twisted channels where grid lines are not aligned with channel directions. This effect is illustrated in Fig. 4, where $r = 16$ mesh is overlapped with $\delta x = 1$ m channel bathymetry. The white double arrow shows a cross section A_C where x-flux passes through. Note that the cross-section does not equal the channel width because mesh and channel boundaries are not aligned. The red arrows represent the minimum face areas $A_{X(\min)}$ within three coarse cells (named *G1-G3*) as suggested by Bruwier et al. (2017). It can be seen that for cell *G1* where an interior macro-structure exists, the minimum area $A_{X(\min)}$ represents a true contraction of channel's cross-sectional area. For *G2* and *G3*, however, using minimum areas leads to a decrease of channel's cross-sectional area, i.e., $(A_{X(\min)})_{G2} + (A_{X(\min)})_{G3} < A_C$. Thus, use of the minimum areas can cause false contractions and give biased estimates of the actual flow areas for narrow channels, which leads to an underestimation of conveyance.

Furthermore, grid alignment along an angled channel boundary – as commonly seen for natural river channels – often generates coarse-grid cells that contain only a few wet subgrid elements. Bruwier et al. (2017) showed that such "barely-wet" cells can be merged into their neighbor grids to reduce model error, but simply merging volumes and areas (or storage and areal porosity) neglects the spatial arrangements of macro-structures. If grid lines are not aligned with flow direction, numerical diffusion is also increased, which further reduces channel conveyance (Hasan et al., 2012; Holleman et al., 2013; Li and Hodges, 2018; Westerink et al., 2008).

2.3.2. Method: Correction on effective area

To handle the issue with grid alignment, we extend the minimum area idea of Bruwier et al. (2017) by replacing face areas A_X, A_Y in Eqs. (7) and (8) with a more general concept of effective areas $A_{X(\text{eff})}$, $A_{Y(\text{eff})}$. The effective areas equal the minimum areas only if they are much smaller than typical cross-sectional areas at the coarse grid scale, (e.g., where an interior severe contraction of cross-section is detected). Otherwise the effective areas $A_{X(\text{eff})}$ and $A_{Y(\text{eff})}$ equal the areas A_X, A_Y provided by upscaling at cell faces, as in Li and Hodges (2019). Formally, the effective area is computed for A_X as:

$$A_{X(\text{eff})} = \begin{cases} A_{X(\min)}, & \text{if } \left(A_{X(\text{med})} - A_{X(\min)}\right) > \gamma\left(A_{X(\max)} - A_{X(\text{med})}\right) \\ A_X, & \text{otherwise} \end{cases} \tag{15}$$

with a similar equation for A_Y. In the above, γ is a model coefficient and the $A_{X(\text{med})}$, $A_{X(\max)}$, $A_{X(\min)}$ are median, maximum and minimum cross-sectional areas in the staggered coarse-grid cell surrounding the face.

These terms are defined for a cell with a grid-coarsening ratio r (i.e., containing r subgrid cells in x direction), which has a set of r different cross-sectional areas $\{A_{X1}, A_{X2}, \dots A_{Xr}\}$ in the x direction. Formally, the coarse-grid cell statistics are:

$$A_{X(\mathrm{med})} = \mathrm{median}_{i=1}^{r}(A_{Xi})$$
$$A_{X(\mathrm{max})} = \mathrm{max}_{i=1}^{r}(A_{Xi})$$
$$A_{X(\mathrm{min})} = \mathrm{min}_{i=1}^{r}(A_{Xi}) \tag{16}$$

The median, minimum and maximum areas are shown in Fig. 4 for the example cells *G1* and *G3*. The coefficient $\gamma > 0$ in Eq. (15) determines when $A_{X(\mathrm{min})}$ can be identified as a true channel contraction.

The present study uses $\gamma = 2$, which identifies a contraction when the difference between median to minimum areas is twice the difference between maximum to median areas. In effect, this occurs when there is a subgrid cross-sectional area that is substantially smaller than would be expected if the areas A_{Xi} were uniformly distributed about the median. Coarse-grid cells *G1* and *G3* in Fig. 4 can be used as illustrative examples. Cell *G3* contains a section of (almost) straight channel boundary, but since the channel direction and grid lines are not aligned, the interior face areas A_{Xi} show (nearly) linear variation along the x axis. Applying Eq. (15) with $\gamma = 2$ yields similar magnitudes for $A_{X(\mathrm{med})} - A_{X(\mathrm{min})}$ and $A_{X(\mathrm{max})} - A_{X(\mathrm{med})}$ and results $A_{X(\mathrm{eff})} = A_X$. This result indicates there is no severe contraction to generate partial blocking effects. For cell *G1*, the A_{Xi} values are the same for most cross sections because channel bank only takes a small region in the upper left corner. However, the existence of a sidewall obstacle leads to a small value for the minimum area, which provides $A_{X(\mathrm{med})} - A_{X(\mathrm{min})} \gg 2\left(A_{X(\mathrm{max})} - A_{X(\mathrm{med})}\right) = 0$. That is, the contraction area is substantially different than expected given the range of the cross-sectional areas on the high side of the median. The effective area in this case is set to the minimum area at the contraction location. The use of Eq. (15) successfully separates a true channel contraction caused by interior macro-structures (*G1*) from a false contraction caused by misalignment between channel and grid lines (*G3*). In Section 4, the selection of $\gamma = 2$ and other possible statistical approaches to identifying contractions are discussed.

2.3.3. Method: Mesh-shifting

For coarse-grid cells containing only a few wet subgrid cells (referred as "barely-wet" or *bw* coarse-grid cells, shown as the white triangle in Fig. 4), a smaller time step is required to maintain stability if the numerical algorithm is strictly CFL limited (Bruwier et al., 2017). To completely eliminate *bw* cells and their time-step constraint, Bruwier et al. (2017) developed a cell-merging technique that merges the *bw* cells with their neighbor coarse-grid cells. A disadvantage of this approach is that it destroys information on the spatial arrangements of the interior macro-structures. Fortunately, *FrehdC* is generally stable for localized velocities exceeding the CFL condition as long as the high velocity cells do not dominate a large contiguous area of the computational domain (Li and Hodges, 2018). Thus, for *FrehdC* an optimum mesh shift can be developed by minimizing the number of, rather than eliminating the area of, the *bw* cells.

The coarse-grid *bw* cells are a result of the relationship between the coarse-grid mesh and the underlying fine-grid topography, which has a number of possible permutations. As illustrated in Fig. 5, shifting the relationship between the coarse-grid mesh and the underlying fine-grid topography can result in different sets of *bw* cells. The coarse grid necessarily has some (0,0) origin whose position on the fine-grid is an arbitrary choice – i.e., *any* fine-grid cell could be chosen as the coarse-grid origin. It follows that a coarse-grid mesh with a coarsening ratio of $r = \Delta x/\delta x = \Delta y/\delta y$ has r unique positions along each of the x and y axes, providing r^2 unique coarse-fine mesh relationships. It is useful to define (p, q) as unique global indexes for the fine grid topography with $p \in \{1 \dots N_{fx}\}$ and $q \in \{1 \dots N_{fy}\}$ where N_{fx} and N_{fy} are the number of fine-grid cells along the x and y axes. Let (p_0, q_0) be an arbitrary baseline origin of the coarse-grid mesh in the fine-grid topography. The possible permutations of the coarse-grid mesh can be denoted as $M_{\zeta,\psi}$, where $\zeta, \psi = \{0, 1, \dots r-1\}$ are shifts of the coarse-grid origin to $(p_0 - \zeta, q_0 - \psi)$.

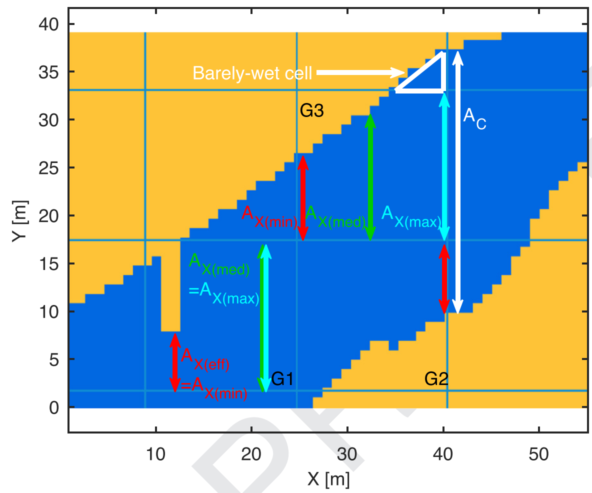

Fig. 4. An illustration of channel's representative cross-sectional area for x-flux, A_C (white double arrow), grid-based minimum areas $A_{X(\mathrm{min})}$ (red arrows), maximum area $A_{X(\mathrm{max})}$ (cyan arrow), median area $A_{X(\mathrm{med})}$ (green arrow) and a barely wet grid cell (white triangle). Blue represents river channel and brown represents land. The mesh shown is created with $r = 16$. Note that by using Eq. (15), the effective area is less than the original face area only in cell *G1*, which also leads to a corresponding decrease in effective volume. (For interpretation of the references to colour in this figure legend, the reader is referred to the web version of this article.) Q2

There are a number of possible ways to define what constitutes a *bw* cell and to quantify the cumulative effects of *bw* cells. For the present purposes, a general definition of a *bw* cell is a coarse-grid cell where the wetted surface area is a small fraction of the coarse-grid cell area, i.e., $A_Z < \beta \Delta x \Delta y$, where $0 < \beta < 1$ is a cut-off fraction. The appropriate value of β depends on the numerical model behavior when $A_Z \ll \Delta x \Delta y$, with $\beta = 0.2$ proving adequate for the tests herein. For *FrehdC*, the optimum coarse-fine mesh relationship is the $M_{\zeta,\psi}$ with the smallest number of *bw* coarse-grid cells.

It can be seen from Fig. 5b that as ζ and ψ change, new *bw* cells are created while existing ones are removed. The mesh-shifting optimization guarantees that the total number of *bw* cells is minimized. The potential issues of creating new *bw* cells are discussed below in Section 4.3. It should be noted that mesh-shifting and the concept of effective area/volume are two methods targeting two different problems incurred during grid-coarsening. Mesh-shifting handles the issue of *bw* cells, which is purely due to misalignment between grid lines and channel boundaries. The effective area/volume are used to simulate effects of interior macro-structures. Although grid alignment issue exists in determining effective area as well (Section 2.3.1), it only affects detailed calculation procedures, not the overall strategy of parametrizing macro-structures. It will be shown in Section 3 that both mesh-shifting and effective area/volume are necessary in reducing model error and alleviating sensitivity of model performance to mesh design.

Fig. 6 provides a flowchart illustrating the relationships between algorithms for mesh shifting, effective area, effective volume, the baseline SB approach, and the traditional roughness representation of microstructure. Mesh-shifting is performed prior to grid-coarsening as a preprocessing step that optimizes the high-resolution topography. The upscaling (grid-coarsening) process provides different sets of subgrid variables for the different methods. Within the scope of the present study, the face volumes V_X, V_Y in Eqs. (7)–(10) are replaced by either $V_{X(\mathrm{eff})}$, $V_{Y(\mathrm{eff})}$ or $V_{X(\mathrm{min})}$, $V_{Y(\mathrm{min})}$ as two different approaches to model the effects of macro-structures and constrain topographic dissipation. The face areas A_X, A_Y are replaced with $A_{X(\mathrm{eff})}$ and $A_{Y(\mathrm{eff})}$. The volume modifications do not affect mass conservation as volumes do not appear

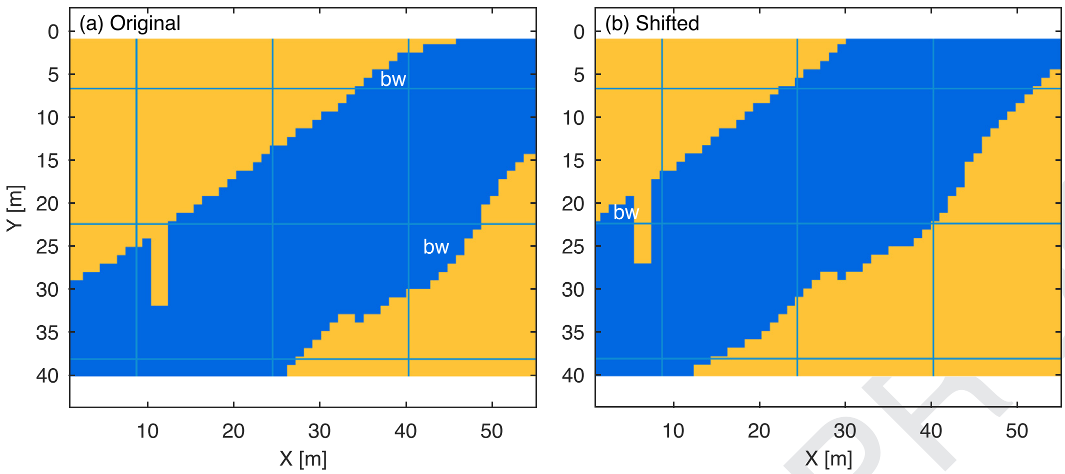

Fig. 5. (a) The background bathymetry used in Fig. 4 with $r = 16$ mesh, which is used as $M_{0,0}$ position. Two *bw* cells are marked. (b) Bathymetry of the same region shifted with $\zeta = 5, \psi = 5$ ($M_{5,5}$). The two original *bw* cells are eliminated but a new one is created.

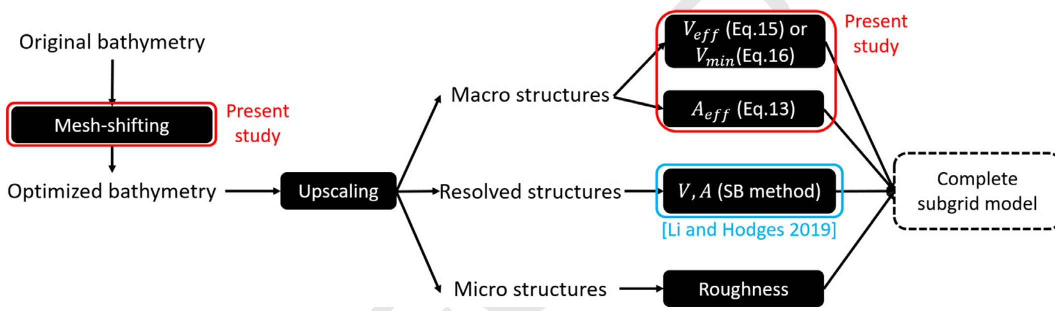

Fig. 6. Flowchart illustrating the relations between different components of a complete subgrid method.

in continuity (Eq. (7)). The area modifications may affect the result of the continuity equation, but they do not change the inherent mass conservation in the method as the volume increment $\Delta\eta A_Z$ remains exactly balanced by the net fluxes through the faces. The test scenarios described in Section 3 are designed to examine model sensitivity to mesh-shifting, effective areas, and effective volumes as compared to the baseline SB case.

Table 1
List of different test scenarios.

Test scenario	Reduce area	Reduce volume	Roughness upscaling
SB	No	No	No
SB-A	Yes (Eq. (15))	No	No
SB-V	No	Yes (Eq. (13))	No
SB-VA	Yes (Eq. (15))	Yes (Eq. (13))	No
SB-V$_\alpha$A	Yes (Eq. (15))	Yes (Eq. (14))	No
SB$_{\mathrm{Volp}}$	No	No	Yes (Volp et al., 2013)

3. Test cases and results

3.1. Straight channel with sidewall obstacle

The above modifications to the governing equations and mesh design are tested on two domains. The first domain is shown in Fig. 7, where two 100 × 100 m square "lakes" are connected with a straight channel of 20 m width. The bottom elevations of the channel and lakes are uniform at 0 m. An object (e.g., bridge pier) with length D is placed on the sidewall of the channel as a subgrid macro-structure. Constant water levels of 0.3 m and 0.35 m are forced at $x = 0$ m and $x = 600$ m respectively. At steady-state, the solution has an overall surface gradient of 8.33×10^{-5}. A fine-grid simulation ($r = 1$) is executed with 0.25 m grid spacing, which is used as the "true solution". The subgrid simulations use coarse-grid spacing of $\Delta x = 20$ m ($r = 80$). The mesh is intentionally designed such that exactly one coarse-grid cell is placed across the channel width and the bridge pier does not intersect with grid faces.

The following (Table 1) includes tests of five model scenarios executed in this study. The scenarios are created by selecting different treatments on macro-structures. The notation SB represents the baseline subgrid method described in Li and Hodges (2019). The new effective subgrid area approach (Eq. (15)) is designated SB-A. The new effective volume approach (Eq. (13)) is named SB-V. Tests implementing both new effective area and volume algorithms are designated SB-VA. Tests with effective area and volume algorithms for additional near-wall dissipation (Eq. (14)) are SB-V$_\alpha$A. For comparison with prior work, the roughness upscaling method of Volp et al. (2013) is applied with the baseline subgrid model and designated as SB$_{\mathrm{Volp}}$.

The steady-state flow rate errors (computed as the difference of in-channel flow rate between test simulation at Δx and reference fine-grid simulation at δx, that is, $Q_{r=80} - Q_{r=1}$) are shown in Fig. 8. Taking flow towards $-x$ direction to be positive, it can be seen that for $D \in \{4, 6, 8, 10, 12, 14\}$ m, the SB-VA scenario minimizes flow rate error. By ignoring the macro-structure and its blocking effects, the SB simulation tends to overestimate flow rate, whereas taking minimal cross-sectional area alone (SB-A) underestimates flow rate because of topographic dissipation. As D increases, the flow rate errors tend to increase for all scenarios, indicating that not all processes caused by the macro-structure are captured by A_{eff} and V_{eff}. Such processes might include mass/momentum exchange between advection and recirculation zones (Fig. 3b) as well as upscaling of bottom roughness (discussed in §4, below). Clearly, SB-VA is an improvement over the SB scenario that uses the subgrid method

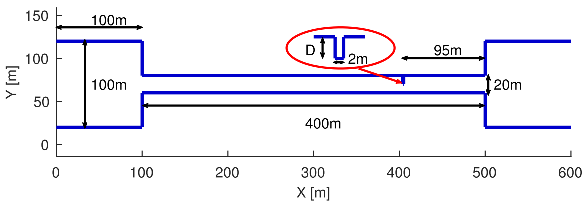

Fig. 7. Top view of the outline of the straight channel computation domain. In the red ellipse is detailed view of regions near the bridge pier. (For interpretation of the references to colour in this figure legend, the reader is referred to the web version of this article.)

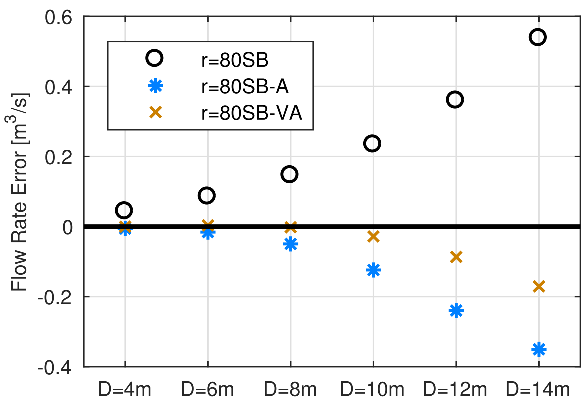

Fig. 8. Steady-state flow rate error in the straight-channel domain (Fig. 7) for various D and subgrid scenarios tested. Positive error indicates overestimation of flow rate. Negative error means underestimation.

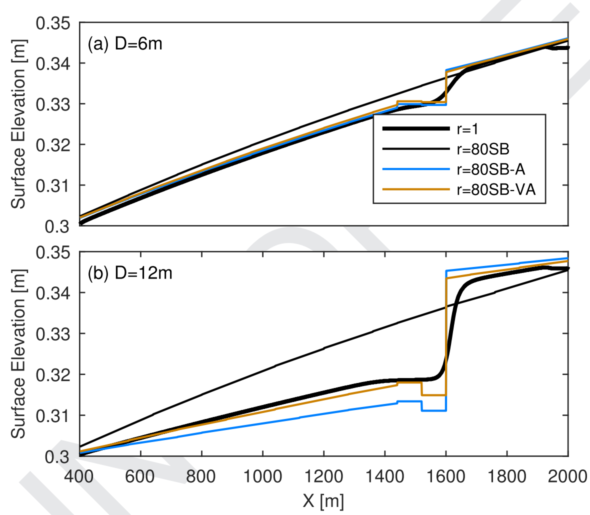

Fig. 9. Profiles of steady-state surface elevations in longitudinal direction of the straight channel for $D = 6$ m and $D = 12$ m.

described in Li and Hodges (2019). Results for the SB-V case (not shown) simply provide an amplification of the overestimation of the SB method.

Fig. 9 shows the steady-state surface elevation profiles in the straight channel. Results for the subgrid scenarios are downscaled following Sanders and Schubert (2019). A severe decline of surface elevation across the bridge pier can be found for the fine-grid simulations, which is caused by the blocking effects from the interior macro-structure. The SB scenarios predict constant surface slope along the entire channel because the macro-structure is completely neglected. Both the SB-A and SB-VA scenarios show a change in surface gradient across the bridge pier. For $D = 6$ m, the difference between these two scenarios is minor. However, for $D = 12$ m the SB-A scenario overestimates the drop

Table 2
List of differences among tested bathymetries.

Bathymetry	Sidewall macro-structures	Number of *bw* cells	Channel bottom
NP	No	Min.	Flat
NPS	No	Max.	Flat
WP	Yes	Min.	Flat
WPB	Yes	Min.	Uneven

of free surface. Although slight overestimation is also found for SB-VA, it provides the best approximation of surface elevation to the fine-grid solution among the three tested scenarios.

3.2. Twisted channel in the Nueces Delta

The second domain (Fig. 10a) is a semi-enclosed tidal-driven marshland. It consists of a “bay” on the east side, a twisted main channel and several well- or poorly-connected shallow lagoons. The boundary shapes of these features are modified from the 1×1 m lidar data of the Nueces Delta, which is a shallow coastal wetland located near the City of Corpus Christi (Texas, USA). The entire Nueces Delta has been modeled in Li and Hodges (2018, 2019). For computational efficiency, the present domain only covers a 480×2000 m section. A grid-coarsening ratio $r = 16$ is used for the Nueces Delta test case. Mesh shifting is applied to minimize the number of *bw* cells, with results as shown in Fig. 11. The mesh with the minimum number of *bw* cells is shown in Fig. 10a as the “No Pier” (NP) case. To test the effect of mesh shifting, a “No Pier Shifted” (NPS) case is designed with the coarse-grid mesh corresponding to the maximum number of *bw* cells. To evaluate the new macro-structure algorithm, three sidewall piers are added to a stretch of the channel (Fig. 10b), creating the “With Piers” (WP) case with exactly the same mesh arrangement as the NP case. To eliminate confounding effects of micro-structure and retain our focus on the macro-structure, the bottom elevations from the real submerged topography are replaced with a uniform value of 0 m throughout the domain for the NP, NPS, and WP cases. To provide insight into the interaction of micro-structure and macro-structure the original submerged topography is maintained in a “With Pier Bathymetry” (WPB) case. A view of the WPB bathymetry in the stretch of channel with the bridge piers is shown in Fig. 10c. The differences among the four test bathymetries are summarized in Table 2. Sinusoidal tide (with range of 0.2 m and period of 24 h) is added along the east boundary for these cases.

For the Nueces Delta test scenarios, the relative flow rate errors across X1 (Fig. 10a) over one tidal period is shown in Fig. 12. One of the challenges of interpreting error behavior is that the two effects of poorly-modeled macro-structure – neglect of partial blocking and topographic dissipation have opposite effects; i.e., the former leads to overestimation of conveyance and the latter an underestimation. Thus, serendipitous cancellation of error can occur, which might result small mean or median error. To avoid such situations, we consider the interquartile range (IQR) to be a more important indicator of model performance than the mean or median error because it reflects the variation of error over the entire simulation period, which increases the chance of capturing model deviations from the reference simulation. For the NP domain with the optimum mesh shift to minimize barely wet cells and without bridge piers (Fig. 12a), no severe channel contraction is detected in the main channel with $\gamma = 2$ (although several contractions are found in the lagoon regions close to the left boundary). The SB-A algorithm has slight higher error than the baseline SB method. Applying effective volume (SB-V) reduces flow rate error compared to SB and SB-A algorithms, whereas the SB-VA scenario produces slightly higher error than SB-V. It should be noted that using effective volume alone (SB-V) does not have much physical significance because Eq. (13) is derived for the cases where topographic dissipation is always associated with change in cross-sectional area, but SB-V shows superior performance to SB-VA in terms of flow rate error, which indicates the existence of additional

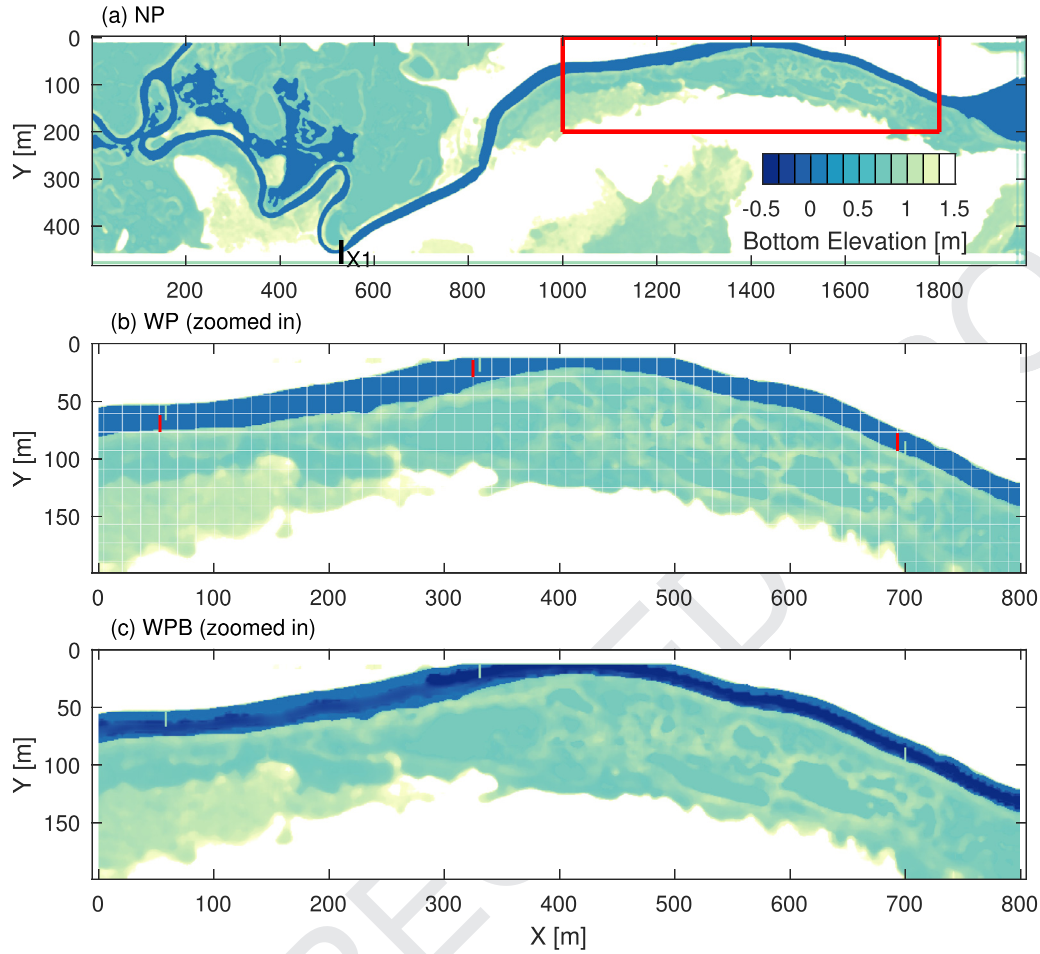

Fig. 10. (a) Bathymetry of the full domain of the Nueces Delta test case NP at 1×1 m resolution. In-channel flow rate is calculated at cross-section *X1*. (b) Details of bridge piers in channel WP within red box of frame (a). The white mesh represents $r = 16$ coarse grid cells. Red lines are cell faces whose effective area $A_{eff} < A$. (c) Details of channel WPB with non-uniform submerged bathymetry (coarse mesh not shown for clarity). (For interpretation of the references to colour in this figure legend, the reader is referred to the web version of this article.)

dissipation processes that are not captured by Eq. (13). This statement is verified by results with SB-V$_\alpha$A, where flow rate error further decreases with the use of reduced volumes for all coarse cells (Eq. (14)). The additional dissipation is likely caused by smoothing the transverse velocity gradient near the channel boundary. The effective volume approach of SB-V$_\alpha$A is also superior to the Volp et al. (2013) model, SB$_{\text{Volp}}$.

The contrast between results with the NP topography (optimized mesh shift) and the NPS topography (poorly-optimized mesh shift) in Fig. 12(a) and (b) is striking. Poor optimization of the mesh (maximizing the barely-wet cells) causes dramatically increased error and IQR across all the methods. A possible reason is increased numerical dissipation when flow enters and exits these additional *bw* cells, which cannot be compensated by any of the subgrid algorithms. These results illustrate the optimization of the mesh is critical to effectively applying subgrid algorithms. It should be noted that despite this sensitivity to the mesh placement, the subgrid method (even with NPS bathymetry) still has its advantage over existing grid-coarsening methods without subgrid parametrization (e.g. Hodges, 2015) that cannot maintain surface connectivity of the main channel at $r = 16$ and completely prevent tidal intrusion into the lagoons (results not shown).

Relative error results for the NP topography seem to imply the SB-V approach is superior to SB-A and the latter algorithm is unnecessary. However, addition of the bridge piers in the WP case, Fig. 12(c), indicates the effects are reversed when the geometry includes significant partial-blocking macro-structure. With the bridge piers included, the SB-VA has the minimum error. The IQR results for the flow error of

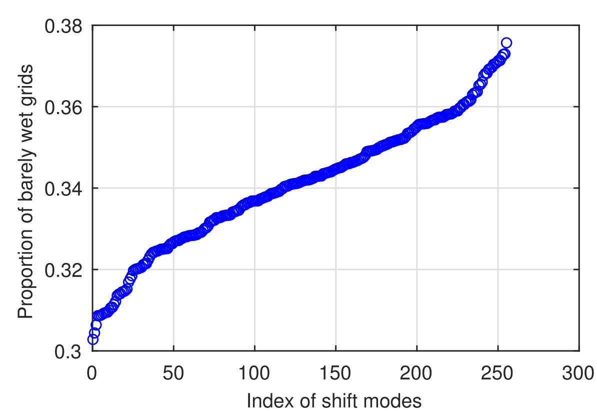

Fig. 11. Proportion of barely-wet (*bw*) cells in all wet cells for the 256 possible shift modes ($r = 16$) for the NP bathymetry. Results displayed in ascending order.

the SB, SB-A, and SB-V$_\alpha$A algorithms are similar, whereas the SB-V has the highest error. That is, when partial-blocking behavior exists, treatments of both flow areas and volumes at channel contractions are important. Flow features are dominated by processes associated with partial-blocking macro-structures, making other dissipation mechanisms of secondary importance. It is useful to consider the temporal evolution of the root-mean square error (RMSE) of the surface elevation for the SB and

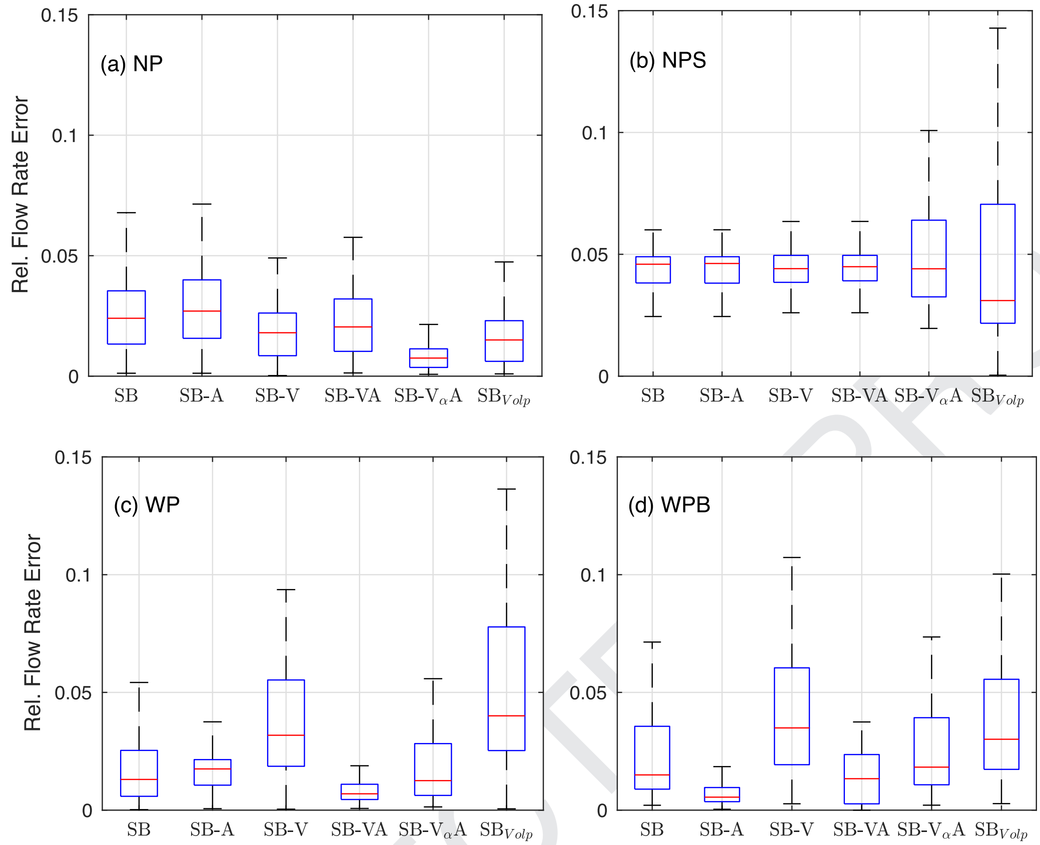

Fig. 12. Relative flow rate error ($|Q_{r=16} - Q_{r=1}|/|Q_{r=1}|$) at cross-section X1 (Fig. 10) over one tidal period for the Nueces Delta test scenarios. The red mark represents the median over one tidal period and the blue box is the interquartile range. (For interpretation of the references to colour in this figure legend, the reader is referred to the web version of this article.)

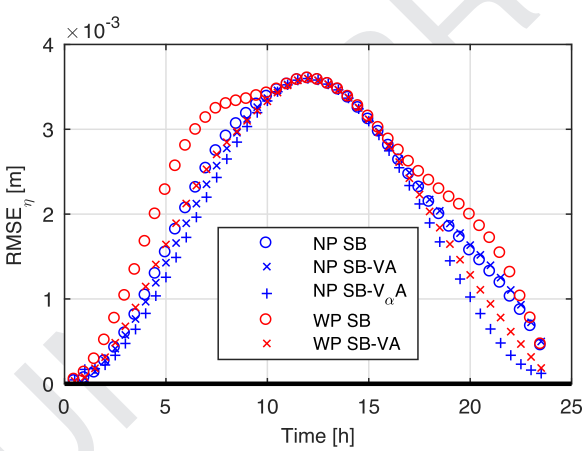

Fig. 13. Temporal variation of surface error for selected NP and WP scenarios.

SB-VA models, as shown in Fig. 13. It can be seen that for both NP and WP bathymetries the SB-VA (and SB-V$_\alpha$A) produces smaller RMSE$_\eta$ errors than the baseline SB method. Note that the RMSEs show periodic variations due to the semi-enclosed nature of the model domain. That is, an initial overestimation of flow rate leads to rapid increase of surface elevation, which then reduces the surface gradients between the open boundary and the interior lagoons, hence reducing flow rates. This behavior restrains further tidal intrusion and slows down the rising of free surface, as is evidenced by the sudden reduction in the rate that error is increasing for the WP SB scenario around 7 h into the simulation towards the end of the rising tide. Furthermore, when the tide falls, since the surface elevation is overestimated, it generates larger surface gradient that drains the lagoons quickly. As a result, the RMSE drops to almost zero at the end of the tidal cycle. This periodic behavior is thus not a result of applying the proposed subgrid method, but the differences between SB and SB-VA errors are certainly caused by the subgrid treatments to the macro-structures.

Non-uniform bottom topography is added to the 1×1 m for the control simulation in case WPB, providing the relative flow rate error behavior shown in Fig. 12(d). Here we see the SB-A algorithms perform best, SB-VA the second best, the SB and SB-V$_\alpha$A being similar and the SB-V and SB$_{\mathrm{Volp}}$ being somewhat worse. The superiority of SB-A over SB-VA indicates variation of bottom elevation induces higher flow resistance that is not represented by A_{eff} and V_{eff}. These results have implications for the importance of upscaling bottom drag, which is beyond the scope of the present study.

A comparison of the spatial distribution of water surface elevations for the WP scenarios provides further insight into the performance of the subgrid algorithms. Here we focus on the simulation during the rising tide ($T = 8$ h), as shown in Fig. 14. The flow rate IQR statistics in Fig. 12 indicate that the SB and SB-A are relatively similar in performance, but here it can be seen that the SB method results in higher in-channel water surface elevations from 600 to 1400 m compared to the $r = 1$ control, the SB-A and the SB-VA. These results indicate that SB allow increased conveyance in the channel compared to the SB-A and SB-VA. Overestimation of conveyance (and surface elevation) is also observed in SB-V. The flooding of the off-channel lagoons (left side of domain) provides another interesting point of comparison. The SB, and SB-V methods have higher water surface elevations than the $r = 1$ control in the off-channel lagoons, indicating there is too much connectivity. The SB-A method has too much blockage in the connections to the lagoons.

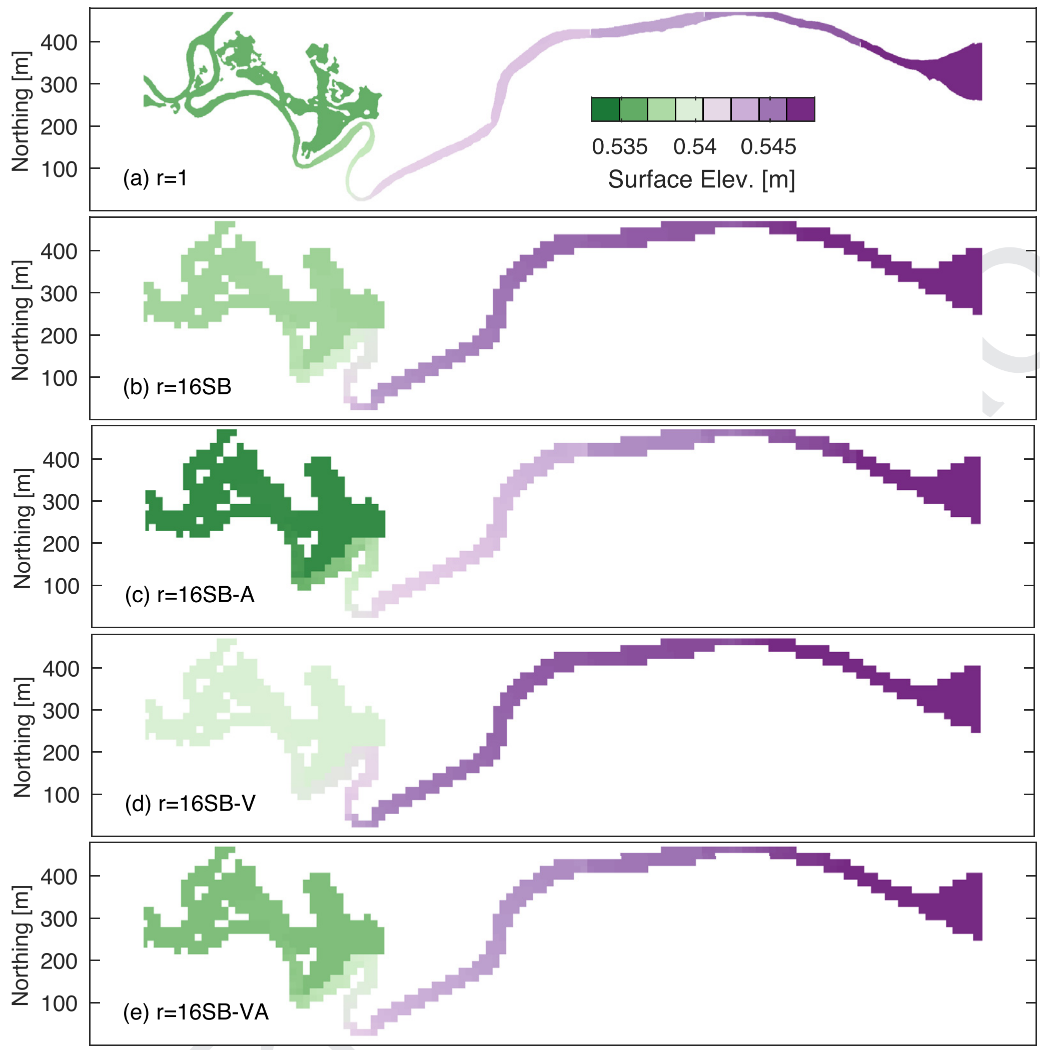

Fig. 14. Surface elevation at $T = 8$ h (corresponds to rising tide) for WP scenarios. Tidal boundary condition enforced on right side of domain.

Overall, the SB-VA method has the best combination of representing connectivity within the lagoon without overestimating conveyance in the channel.

4. Discussion

The results above show that subgrid models characterized by both effective areas and effective volumes can improve the modeling of flow effects caused by macro-structures in 2D tidal marsh models. In general, the effective area approach reduces the modeled flow cross-section due to macro-structures that are interior to a coarse-grid cell (whose neglect otherwise leads to overestimation of conveyance). Unfortunately the effective area approach, by itself, leads to an overestimation of topographic dissipation – i.e., the tendency of tortuous flow paths to dilute the effects of pressure gradients driving the flow. The effective volume approach acknowledges that flow volumes “hiding out” behind obstructions are not affected by driving pressure gradients, and hence applying a smaller effective volume counters the tendency of the effective area approach to overestimate topographic dissipation. The effective area method used herein is an extension of Bruwier et al. (2017) by incorporating a conditional criterion (Eq. (15)) that identifies and removes “false” channel contraction caused by misalignment between channel and grids. Room for further improving this approach is discussed in Section 4.1. Limitations and assumptions for the new effective volume method are discussed in detail in Section 4.2. A challenging problem is that macro-structure effects are inherently sensitive to the coarse-grid mesh placement, which is shown to significantly alter the effectiveness of the subgrid models. The sensitivity of model results to mesh-shifting and its implications are discussed in Section 4.3. Finally, the model tests herein were focused on side-wall macro-structure that caused flow blockages, as characterized by bridge piers in Figs. 7 and 10. For simplicity, these test cases used uniform bottom bathymetry with a uniform bottom roughness across all coarse and fine-grid cells. The interaction of the subgrid models with the more general macro-structure of non-uniform (but non-blocking) bathymetry and upscaling of micro-structure remains to be explored.

4.1. On the effective area

Clearly, the idealized effective area strictly applies only to Eq. (15) for a single interior sidewall obstacles that laterally contract the cross-sectional area. Macro-structures in real marshes have more complex geometries and form a variety of different blocking patterns and flow paths in the cell interior. To handle this increased complexity, other statistical properties might also be used to distinguish true and false channel contractions – which implies broad avenues for future research. Although the concept of simulating partial blocking as a reduction of cell face area is arguably valid for more complex geometry, developing well-grounded mathematical expressions of $A_{X(\mathrm{eff})}$ and $A_{Y(\mathrm{eff})}$ for such cases is beyond the scope of the present research. Similarly, herein we have not tested model sensitivity to the choice of parameter γ in Eq. (15): we consider this parameter to be merely an interim step showing the approach of Bruwier et al. (2017) – that used minimum areas – can be improved by a more flexible formulation. That is, this research demonstrates that modifications of face areas to represent subgrid features can be extended beyond the minimum area approach, but determining the optimum approach will require more detailed study and we doubt that the γ discriminator of Eq. (15) will prove sufficiently robust for a wide variety of geometries.

4.2. On the effective volume

The proposed model for effective volume introduces two substantial idealizations. First, the advection and recirculation zones are assumed completely separated (Fig. 3b). Second, topographic dissipation caused by near-wall velocity gradient is not parametrized. The separation of the advection and recirculation zones in V_{eff} implies that the mixing layer between the two zones and the associated turbulent mixing processes are neglected (Han et al., 2017). Furthermore, for simplicity the size of V_{eff} in any cell is a constant that is independent of the local velocity, which clearly is not a direct representation of the complex flow physics around an object. For tidal-driven flow that reverses regularly, the locations of the recirculation zones also depend on flow direction. It remains to be seen whether adding further complexities associated with the local flow field (direction and velocity) can improve a subgrid model.

Fig. 12 a implies that additional dissipation processes exist in narrow twisted channels, which are likely caused by smoothing of velocity gradients near the channel boundaries. From Fig. 12c, as expected, this near-wall dissipation cannot be adequately modeled using an effective volume concept similar to the one for recirculation zones, e.g., Eq. (14), because such dissipation is generated through different mechanisms, i.e., *not* through a sudden contraction and the associated recirculation region. The dissipation near channel boundaries will be related to the interaction of the micro-structure, the sidewall boundary layer, and macro-structure geometry, which will require future studies at finer than the $\delta x = 1$ m resolution used herein as the "true solution" for evaluating model performance. Similarly, including sidewall effects requires considering 3D flow effects (Jeon et al., 2018; Monsalve et al., 2017), which cannot be handled with the present model. To fully resolve the near-wall velocity gradient and quantify all complex mechanisms occurring there, experimental data (e.g. Velickovic et al., 2017) or full 3D non-hydrostatic simulation results (e.g. Munoz and Constantinescu, 2018) are likely required. Thus we consider the approach using the α parameter in Eq. (14) to be simply a demonstration that some further geometric dependency of the effective volume might be desirable, but optimization of the proposed α in the present model structure is unlikely to provide further insight.

The difficulty in characterizing the size of effective volume implies a key theoretical challenge, which is to quantify how the geometry of an arbitrary macro-structure affects flow. Both the mixing layer and boundary layer are affected by the geometry of the macro-structures (Babarutsi et al., 1989; Li and Djilali, 1995). However, for shallow coastal marshes with wetting/drying, macro-structures can vary over large spatial and temporal scales. Even if the detailed physical processes near channel boundaries can be resolved at sufficiently fine resolution, a robust quantification of macro-structures is still required for upscaling. The present study simplifies macro-structures to pier-like sidewall obstacles, whose primary effect is a contraction of channel's cross-sectional area. This research illustrates the need for a general mathematical formulation for upscaling geometry effects on flow and turbulence from measurable topography (macro-scale structures) to practical coarse-grid model scales.

4.3. Sensitivity to mesh design

The results comparing the optimum mesh (NP) and the unoptimized mesh (NPS) illustrate the sensitivity of model results to mesh placement (Fig. 12a and b). A similar observation is found in Bruwier et al. (2017). In the present work, a major cause for the increase of flow rate error with the NPS bathymetry is that the barely-wet (*bw*) cells for the unoptimized mesh are typically near the channel boundaries. Where the boundary is at an angle to the grid mesh an inflow in the x direction into a *bw* cell must be shifted to an outflow in the y direction (and vice versa), which enhances local topographic dissipation and reduces channel conveyance (Li and Hodges, 2018).

The NPS mesh also has increased error where upscaling blocks some *bw* areas in channel networks. This occurs because complex channel networks may have multiple disconnected water regions within a single coarse-grid cell. In the baseline upscaling approach (Li and Hodges, 2019) the disconnected sub-regions with smaller wet areas in a single cell are represented as dry land. This simplification is a necessary limitation for an upscaling method that maintains the blockages to surface connectivity associated with subgrid features, but inevitably leads to local underestimation of cell storage for some *bw* cells. As a result, minimization of *bw* cells for the NP model also minimizes loss of volume in upscaling, which reduces the discrepancy with the fine-grid results. For example, the NP and NPS bathymetries at $r = 16$ show reductions of 0.03% and 2.18% volume, repectively (compared to $r = 1$ bathymetry) for a simple uniform surface elevation of 0.4 m.

We recommend minimizing the number of *bw* cells as a simple pre-processing step for *any* subgrid algorithm. However, it should be noted that our mesh-shifting guarantees global minimization of *bw* cells for a selected inundation level, but not necessarily local optimization across all possible levels. A coarse-grid cell that would be classified as *bw* at a particular water surface elevation might be entirely inundated at higher elevation; thus, there remains an open question as to how to optimize a coarse-grid mesh over a range of inundation levels, an effort that might require an adaptive mesh-optimization routine.

5. Conclusions

Porosity-based subgrid models show great potential for efficient simulations of hydrodynamics and salinity transport at shallow coastal marshes. But such models often neglect effects of subgrid-scale interior macro-structures, which makes their performance sensitive to mesh design. The present study focuses on detecting and parametrizing subgrid-scale sidewall macro-structures in narrow twisted channels, reproducing their effects using coarse-grid hydrodynamic models and reducing model sensitivity to mesh design. Three novel strategies are developed: (1) a mesh-shifting procedure that optimizes mesh design by minimizing the number of partially-wet coarse-grid cells, i.e., coarse cells with only a few wet subgrid elements, (2) use of the effective grid-face areas $A_{X(\mathrm{eff})}$ and $A_{Y(\mathrm{eff})}$ to simulate partial-blocking effects of the macro-structures, and (3) use of the effective volumes $V_{X(\mathrm{eff})}$ and $V_{Y(\mathrm{eff})}$ to reduce topographic dissipation, which is caused by smoothing of transverse velocity gradient at coarse scale. These strategies are implemented into the existing subgrid model in the *FrehdC* code (Li and Hodges, 2019) and are tested on both synthetic and real bathymetries. Model evaluation is performed by comparing coarse-grid to fine-grid simulation results.

In the synthetic test case, a combined use of A_{eff} and V_{eff} minimizes error in flow rate and surface elevation for all tested dimensions of the macro-structure. In the realistic Nueces Delta computation domain, mesh-shifting is demonstrated as necessary to reducing model error. In conjunction with the mesh-shifting method, the combined A_{eff} and V_{eff} subgrid models provide the best approximation of the fine-scale surface elevations and flow rates. When severe contractions are absent, model performance is affected by additional dissipation processes that are not included in V_{eff}. The main advantage of the proposed treatments is the direct connection to idealized physical processes and the channel geometry, which makes it possible to develop analytical expressions for effects of macro-structures. We believe these advances are applicable over a broad range of shallow flows and can be used to limit the extensive efforts that are otherwise required when the drag coefficient is taken as a local calibration coefficient. Future studies are still required to parametrize processes not included in the present model, such as dissipation near channel boundaries and the effects of non-uniform submerged channel bathymetry. This research shows there is an urgent need for a mathematical framework to characterize and quantify the geometry of a variety of macro-structure scales, orientations, and topologies based on measurable data and their statistics.

Declaration of Competing Interest

The authors declare that they have no known competing financial interests or personal relationships that could have appeared to influence the work reported in this paper.

Supplementary material

Supplementary material associated with this article can be found, in the online version, at doi:10.1016/j.advwatres.2019.103465.

References

Azinfar, H., Kells, J.A., 2009. Flow resistance due to a single spur dike in an open channel. J. Hydraul. Res. 47, 755–763. https://doi.org/10.3826/jhr.2009.3327.

Babarutsi, S., Ganoulis, J., Chu, V., 1989. Experimental investigation of shallow recirculating flows. J. Hydraul. Eng. 115(7), 906–924.

Bates, P.D., 2000. Development and testing of a subgrid-scale model for moving-boundary hydrodynamic problems in shallow water. Hydrol. Process. 14, 2073–2088.

Bruwier, M., Archambeau, P., Erpicum, S., Pirotton, M., Dewals, B., 2017. Shallow-water models with anisotropic porosity and merging for flood modelling on cartesian grids. J. Hydrol. (Amst.) 554, 693–709. https://doi.org/10.1016/j.jhydrol.2017.09.051.

Casas, A., Lane, S.N., Yu, D., Benito, G., 2010. A method for parameterising roughness and topographic sub-grid scale effects in hydraulic modelling from liDAR data. Hydrol. Earth Syst. Sci. 14, 1567–1579. https://doi.org/10.5194/hess-14-1567-2010.

Casulli, V., 1990. Semi-implicit finite-difference methods for the 2-dimensional shallow-water equations. J. Comput. Phys. 86, 56–74.

Casulli, V., Cattani, E., 1994. Stability, accuracy and efficiency of a semi-implicit method for three-dimensional shallow water flow. Comput. Math. Appl. 27 (4), 99–112.

Cea, L., Legout, C., Darboux, F., Esteves, M., Nord, G., 2014. Experimental validation of a 2D overland flow model using high resolution water depth and velocity data. J. Hydrol. (Amst.) 513, 142–153. https://doi.org/10.1016/j.jhydrol.2014.03.052.

Cheng, N.S., 2015. Resistance coefficients for artificial and natural coarse-bed channels: alternative approach for large-scale roughness. J. Hydraul. Eng. 141(2), 04014072. https://doi.org/10.1061/(ASCE)HY.1943-7900.0000966.

D'Alpaos, L., Defina, A., 2007. Mathematical modeling of tidal hydrodynamics in shallow lagoons: a review of open issues and applications to the venice lagoon. Comput. Geosci. 33, 476–496. https://doi.org/10.1016/j.cageo.2006.07.009.

Defina, A., 2000. Two-dimensional shallow flow equations for partially dry areas. Water Resour. Res. 36 (11), 3251–3264.

Defina, A., D'Alpaos, L., Matticchio, B., 1994. A new set of equations for very shallow water and partially dry areas suitable to 2D numerical models. Modelling Flood Propagation over Initially Dry Areas, American Society of Civil Engineers: New York, 72–81.

Duan, Y., Liu, Z., Chen, Y., Zhu, D., 2017. Improved 2D shallow water model able to capture the effects of complex bathymetric features through their subgrid modeling. Hydraul. Eng. 143 (2), 04016081. https://doi.org/10.1061/(ASCE)HY.1943-7900.0001246.

Guinot, V., Delenne, C., Rousseau, A., Boutron, O., 2018. Flux closures and source term models for shallow water models with depth-dependent integral porosity. Adv. Water Resour. 122, 1–26. https://doi.org/10.1016/j.advwatres.2018.09.014.

Guinot, V., Sanders, B.F., Schubert, J.E., 2017. Dual integral porosity shallow water model for urban flood modelling. Adv. Water Resour. 103, 16–31. https://doi.org/10.1016/j.advwatres.2017.02.009.

Han, L., Mignot, E., Riviere, N., 2017. Shallow mixing layer downstream from a sudden expansion. J. Hydraul. Eng. 143(5), 04016105. https://doi.org/10.1061/(ASCE)HY.1943-7900.0001274.

Hasan, G.M.J., van Maren, D.S., Cheong, H.F., 2012. Improving hydrodynamic modeling of an estuary in a mixed tidal regime by grid refining and aligning. Ocean Dyn. 62, 395–409. https://doi.org/10.1007/s10236-011-0506-4.

Hodges, B.R., 2004. Accuracy order of crank-nicolson discretization for hydrostatic free surface flow. ASCE J. Eng. Mech. 130 (8), 904–910. https://doi.org/10.1061/(ASCE)0733-9399(2004)130:8(904).

Hodges, B.R., 2014. A new approach to the local time stepping problem for scalar transport. Ocean Modell. 77, 1–19. https://doi.org/10.1016/j.ocemod.2014.02.007.

Hodges, B.R., 2015. Representing hydrodynamically important blocking features in coastal or riverine lidar topography. Nat. Hazards Earth Syst. Sci. 15, 1011–1023. https://doi.org/10.5194/nhess-15-1011-2015.

Hodges, B.R., Imberger, J., Saggio, A., Winters, K., 2000. Modeling basin-scale internal waves in a stratified lake. Limnol. Oceanogr. 45 (7), 1603–1620.

Hodges, B.R., Rueda, F.J., 2008. Semi-implicit two-level predictor-corrector methods for non-linearly coupled, hydrostatic, barotropic/baroclinic flows. Int. J. Comut. Fluid Dyn. 22 (9), 593–607. https://doi.org/10.1080/10618560802353389.

Holleman, R., Fringer, O., Stacey, M., 2013. Numerical diffusion for flow-aligned unstructured grids with application to estuarine modeling. Int. J. Numer. Methods Fluids https://doi.org/10.1002/fld.3774.

Horritt, M.S., Bates, P.D., 2001. Effects of spatial resolution on a raster based model FO flood flow. J. Hydrol. (Amst.) 253, 239–249.

Horritt, M.S., Bates, P.D., Mattinson, M.J., 2006. Effects of mesh resolution and topographic representation in 2D finite volume models of shallow water fluvial flow. J. Hydrol. (Amst.) 329, 306–314. https://doi.org/10.1016/j.jhydrol.2006.02.016.

Inoue, M., Park, D., Justic, D., Wiseman, W.J., 2008. A high-resolution integrated hydrology-hydrodynamic model of the barataria basin system. Environ. Modell. Softw. 23, 1122–1132. https://doi.org/10.1016/j.envsoft.2008.02.011.

Jeon, J., Lee, J.Y., Kang, S., 2018. Experimental investigation of three-dimensional flow structure and turbulent flow mechanisms around a nonsubmerged spur dike with a low length-to-depth ratio. Water Resour. Res. 54, 3530–3556. https://doi.org/10.1029/2017WR021582.

Katul, G., Wiberg, P., Albertson, J., Hornberger, G., 2002. A mixing layer theory for flow resistance in shallow streams. Water Resour. Res. 38 (11), 1250. https://doi.org/10.1029/2001WR000817.

Lane, S.N., 2005. Roughness - time for a re-evaluation? Earth Surf. Process. Landf. 30. 251–251 10.1002/esp.1208.

Launder, B.E., Spalding, D.B., 1974. The numerical computation of turbulent flow computer methods. Comput. Methods Appl. Mech. Eng. https://doi.org/10.1016/0045-7825(74)90029-2.

Li, X., Djilali, N., 1995. On the scaling of separation bubbles. JSME Int. J. Ser. B 38(4), 541–548.

Li, Z., Hodges, B.R., 2018. Model instability and channel connectivity for 2D coastal marsh simulations. Environ. Fluid Mech. https://doi.org/10.1007/s10652-018-9623-7.

Li, Z., Hodges, B.R., 2019. Modeling subgrid-scale topographic effects on shallow marsh hydrodynamics and salinity transport. Adv. Water Resour. https://doi.org/10.1016/j.advwatres.2019.05.004.

Matte, P., Secretan, Y., Morin, J., 2017. Hydrodynamic modeling of the St. Lawrence fluvial estuary I: model setup, calibration, and validation. J. Waterw. Port Coast. Ocean Eng. 143(5), 04017010. https://doi.org/10.1061/(ASCE)WW.1943-5460.0000397.

Monsalve, A., Yager, E.M., Schmeeckle, M.W., 2017. Effects of bed forms and large protruding grains on near-bed flow hydraulics in low relative submergence conditions. J. Geophys. Res. Earth Surf. 122, 1845–1866. https://doi.org/10.1002/2016JF004152.

Munoz, D.H., Constantinescu, G., 2018. A fully 3-D numerical model to predict flood wave propagation and assess efficiency of flood protection measures. Adv. Water Resour. 122, 148–165. https://doi.org/10.1016/j.advwatres.2018.10.014.

Ozgen, I., Liang, D., Hinkelmann, R., 2016a. Shallow water equations with depth-dependent anisotropic porosity for subgrid-scale topography. Appl. Math. Model. 40, 7447–7473. https://doi.org/10.1016/j.apm.2015.12.012.

Ozgen, I., Teuber, K., Simons, F., Liang, D., Hinkelmann, R., 2015. Upscaling the shallow water model with a novel roughness formulation. Environ. Earth Sci. 74, 7371–7386. https://doi.org/10.1007/s12665-015-4726-7.

Ozgen, I., Zhao, J.H., Liang, D.F., Hinkelmann, R., 2016b. Urban flood modeling using shallow water equations with depth-dependent anisotropic porosity. J. Hydrol. (Amst.) 541, 1165–1184. https://doi.org/10.1016/j.jhydrol.2016.08.025.

Powell, D.M., 2014. Flow resistance in gravel-bed rivers: progress in research. Earth Sci. Rev. 136, 301–338. https://doi.org/10.1016/j.earscirev.2014.06.001.

Rueda, F.J., Sanmiguel-Rojas, E., Hodges, B.R., 2007. Baroclinic stability for a family of two-level, semi-implicit numerical methods for the 3d shallow water equations. Int. J. Numer. Methods Fluids 54 (3), 237–268. https://doi.org/10.1002/fld.1391.

Sanders, B.F., Schubert, J.E., 2019. PRIMO: parallel raster inundation model. Adv. Water Resour. 126, 79–95. https://doi.org/10.1016/j.advwatres.2019.02.007.

Sanders, B.F., Schubert, J.E., Gallegos, H.A., 2008. Integral formulation of shallow-water equations with anisotropic porosity for urban flood modeling. J. Hydrol. (Amst.) 362, 19–38. https://doi.org/10.1016/j.jhydrol.2008.08.009.

Sehili, A., Lang, G., Lippert, C., 2014. High-resolution subgrid models: background, grid generation, and implementation. Ocean Dyn. 64, 519–535. https://doi.org/10.1007/s10236-014-0693-x.

Shin, G., 2016. A subgrid approach for unresolved topography in shallow water hydrodynamic modeling. Ph.D. thesis. University of Texas at Austin.

Velickovic, M., Zech, Y., Soares-Frazao, S., 2017. Steady-flow experiments in urban areas and anisotropic porosity model. J. Hydraul. Res. 55:1, 85–100. https://doi.org/10.1080/00221686.2016.1238013.

Volp, N.D., van Prooijen, B.C., Stelling, G.S., 2013. A finite volume approach for shallow water flow accounting for high-resolution bathymetry and roughness data. Water Resour. Res. 49, 4126–4135. 10:1002/wrcr.20324.

Wadzuk, B.M., Hodges, B.R., 2009. Hydrostatic versus nonhydrostatic euler-equation modeling of nonlinear internal waves. ASCE J. Eng. Mech. 135 (4), 1069–1080. https://doi.org/10.1061/(ASCE)0733-9399(2009)135:10(1069).

Westerink, J.J., Luettich, R.A., Feyen, J.C., Atkinson, J.H., Dawson, C., Roberts, H.J., Powell, M.D., Dunion, J.P., Kubatko, E.J., Pourtaheri, H., 2008. A basin- to channel-scale unstructured grid hurricane storm surge model applied to southern louisiana. Mon. Weather Rev. 136, 833–864. https://doi.org/10.1175/2007MWR1946.1.

Wu, G., Shi, F., Kirby, J.T., Mieras, R., Liang, B., Li, H., Shi, J., 2016. A pre-storage, subgrid model for simulating flooding and draining processes in salt marshes. Coast. Eng. 108, 65–78. https://doi.org/10.1016/j.coastaleng.2015.11.008.

Zacharias, I., Gianni, A., 2008. Hydrodynamic and dispersion modeling as a tool for restoration of coastal ecosystems. application to a re-flooded lagoon. Environ. Modell. Softw. 23, 751–767. https://doi.org/10.1016/j.envsoft.2007.09.007.